RSC Advances

PAPER

View Article Online
View Journal | View Issue

Cite this: *RSC Adv.*, 2020, **10**, 9693

Facile fabrication of bimetallic Fe–Mg MOF for the synthesis of xanthenes and removal of heavy metal ions†

W. S. Abo El-Yazeed, *[ab] Y. G. Abou El-Reash,[a] L. A. Elatwy[a] and Awad I. Ahmed *[a]

This work reported the preparation of Mg-MOF, Fe-MOF and Fe–Mg MOF by a solvothermal technique and their characterization with FT-IR, XRD, SEM, EDS, TEM and S_{BET} analyses. The nanoparticle diameter ranged from 3.1 to 10.9 nm. The acidity of the MOFs was measured by nonaqueous potentiometric titration of *n*-butylamine. It was observed that the formation of a bimetallic MOF sharply increases the surface acidity and the catalytic activity. The catalytic results of the Fe–Mg MOF catalyzing the synthesis of 14-aryl-14-*H*-dibenzo[*a*,*j*]xanthenes in comparison with those of parent MOFs showed a higher yield of the desired product in a lower time and among various Fe : Mg, the (0.6 : 1) Fe–Mg MOF showed the highest catalytic activity and acidity. Even after the 4th run, the Fe–Mg MOF catalyst still maintained nearly the initial catalytic activity. The adsorption performance of Mg-MOF, Fe-MOF and Fe–Mg MOF was evaluated by batch experiments. The effect of contact time, the solution pH, the adsorbent dose and the initial concentration of the heavy metal ions was discussed. It was found that the capacity of the bimetallic Fe–Mg MOF for Pb(II), Cu(II) and Cd(II) adsorption was higher than that of the Mg-MOF and Fe-MOF, the kinetic data followed the pseudo-second-order kinetic model and the isothermal data obeyed the Langmuir isotherm model. The mechanism of the removal of the heavy metal ions was discussed.

Received 8th December 2019
Accepted 28th February 2020

DOI: 10.1039/c9ra10300g

rsc.li/rsc-advances

1. Introduction

Metal–organic frameworks (MOFs) are a class of compounds constructed by the coordination of clusters or metal ions with organic ligands to compose one, two, or three-dimensional pore structures.[1] Recently, MOFs have received great attention owing to their excellent properties, such as versatile porous structures and numerous potential applications.[2] MOFs are unique and different to other traditional porous solids owing to their interesting properties. These include a simple composition that is easy to prepare compared with zeolites,[3] the presence of coordinative unsaturated active canters, tunable pore structures and ultrahigh surface area.[4] Moreover, MOFs have an important advantage that various frameworks can be formed by the participation of several metal cations.[5] MOFs can be synthesized with specific properties to improve their performances in reaching the desired targets by deliberately and systematically setting their functionalities and structures; for example, the surface area, pore size and/or shape can be controlled by varying the connectivity of the cations and the type of the organic ligands.[6] MOFs have been used in different potential applications as drug delivery,[7] catalytic reactions,[8] sensing[9] and gas adsorption/separation.[10]

Xanthenes compounds are considered as one of the most important organic compounds due to their importance in the formation of biologically active compounds such as blood palette aggregation inhibitor drugs, calcium channel blocker, antibacterial, antiviral, anti-inflammatory, antihypertensive and antitumor. They are also very useful in laser technologies, fluorescent materials for visualization of biomolecules, dyes and photodynamic therapy.[11] Moreover, several polycyclic compounds containing xanthene skeleton have been isolated from natural sources as plant species for their prospective bio-activity. Various methods for the formation of xanthenes derivatives have been reported in the literature.[12,13] Numerous catalysts have been used in the preparation of xanthene, for example, Fe_3O_4-HAD-SO_3H,[14] sulfated starch,[15] ZrO_2,[16] WO_x/ZrO_2 (ref. 17) and sulfamic acid/Cr-MIL-101.[8] Most of the preparation methods suffer from some drawbacks such as constraints of catalyst reusability, separation of pure products, difficult workup, use of hazardous solvents and prolonged reaction times.

Recently; MOFs have received great attention in adsorption of heavy metal ions owing to unique structural features that are not found in other porous materials.[8] In general, the elastic and extremely porous structures of MOFs facilitate the diffusion of the guest ions or molecules easily into the bulk structure. Also; both the size and shape of the formed pores help in increasing

[a]*Chemistry Department, Faculty of Science, Mansoura University, Mansoura, Egypt. E-mail: dr_ws2008@mans.edu.eg; dr.ws20087@gmail.com; awahmed@mans.edu.eg*
[b]*Department of Chemistry, College of Sciences and Humanities in Al-Kharj, Prince Sattam Bin Abdulaziz University, Al-Kharj 11942, Saudi Arabia*

† Electronic supplementary information (ESI) available. See DOI: 10.1039/c9ra10300g

the selectivity of adsorbing definite ions or molecules. These distinct advantages make MOFs ideal sorbents in solid phase extraction of heavy metals.[18] It was reported by the World Health Organization (WHO) in 2008 that the maximum contaminant level (MCL) of lead in drinking water was 10 μg L^{-1}. Consequently, numerous techniques were applied for the removal of heavy metal ions from environmental samples, including membrane filtration,[19] ion exchange[20] and/or adsorption.[21] Adsorption technology is preferred in comparison to the other traditional techniques due to its superior efficiency and easy application.[22] Various adsorbents have been used such as activated carbon,[23] zeolite,[24] ion imprinted polymer[25] and carbon nanotubes.[26] However, the applications of these adsorbents have shown some weakness. Therefore some studies have been carried out with the intention of developing new, cheap and sustainable adsorbents for the removal of heavy metal ions from wastewaters. These adsorbents should possess high affinity, selectivity and capacity towards these metals.

Here, bimetallic Fe–Mg MOFs with different Fe : Mg molar ratios have been successfully synthesized *via* the solvothermal method. Fe–Mg MOFs was utilized for the removal of Pb(II), Cd(II) and Cu(II) from aqueous solution and as a solid Lewis acid catalyst for the synthesis of 14-aryl-14-*H*-dibenzo[*a*,*j*]xanthenes. The structure of the bimetallic Fe–Mg MOF was elucidated by (FT-IR), (XRD), (SEM) and (TEM) analyses.

2. Experimental

2.1. Materials

$Mg(NO_3)_2 \cdot 6H_2O$, $Fe(NO_3)_3 \cdot 9H_2O$, terephthalic acid and dimethylformamide (DMF) from Sigma Aldrich. Lead nitrate, copper nitrate and cadmium nitrate which provided by BDH. *N*-Butylamine, acetonitrile, ethyl acetoacetate, benzaldehyde, urea and 2-naphthol were used as received.

2.2. Preparation of MOFs

Fe–Mg bimetallic organic frameworks with different molar ratios of Fe^{3+} : Mg^{2+}, (0.6 : 1 and 1 : 1), were synthesized as reported previously.[27] 1 mmol of $Mg(NO_3)_2 \cdot 6H_2O$, $Fe(NO_3)_3 \cdot 9H_2O$ (0.6 mmol or 1 mmol) and 1 mmol of terephthalic acid (H_2BDC) were dissolved in 10 mL of DMF under constant stirring. The mixture was blended completely and heated at 120 °C in a Teflon-lined autoclave for 8 h. Then, the suspension was cooled gradually to room temperature, collected by centrifugation, washed with DMF several times and dried at 120 °C under vacuum. The resulted brown powder were denoted as (0.6 : 1) Fe–Mg MOF and (1 : 1) Fe–Mg MOF.

In the same manner, monometallic Fe-MOF and Mg-MOF were synthesized using only $Fe(NO_3)_3 \cdot 9H_2O$ or $Mg(NO_3)_2 \cdot 6H_2O$ as the metal precursor.

2.3. Instrumentation

The FTIR spectra were measured using Thermo SCIENTIFIC (NICOLET iS10) FTIR spectrometer from Thermo Electron Corporation in the range 400–4000 cm^{-1} for a sample of 2 mg diluted with 200 mg KBr. Powder X-ray diffraction was performed using PW150 (Philips) using Cu Kα radiation source and Ni filter. The instrument was operated at a voltage of 40 kV and a current of 45 mA. TEM (transmission electron microscopy) images were obtained using a JEOL-JEM-2100 transition-electron-microscope. SEM (scanning electron microscopy) and EDS (energy dispersive X-ray spectroscopy) images for surface morphological evaluation and composition were obtained using JEOL-JSM-6510LV scanning-electron-microscope, Japan. The porosity of the MOF materials and BET surface area are examined by N_2 adsorption/desorption analysis at −196 °C.

2.4. Surface acidity measurements

The surface acidity of MOFs have achieved by nonaqueous titration of 0.03 g of MOF suspended in 10 mL acetonitrile with (0.025 N) *n*-butylamine at 0.005 mL min^{-1}, which is a basic molecule suitable for the titrating strong acid and medium sites present on the surface of the catalysts.[28] The various electrode potential values were measured using a double-junction electrode of an Orion 420 digital A model.

2.5. Catalytic activity

A mixture of (1 mmol) benzaldehyde, (2 mmol) 2-naphthol, and (0.05 g) MOF was placed in a round bottom flask in an oil bath and fitted to a condenser at 120 °C for 2 h for the synthesis of 14-aryl-14-*H*-dibenzo[*a*,*j*]xanthenes. The progress in the reaction was adjusted using TLC. After cooling, the reaction mixture was placed onto crushed ice and mixed for a few minutes. The product was filtrated, washed with cold water and after that recrystallized by using ethanol to yield the pure product which was calculated as follows:

$$\text{Yield (wt\%)} = \frac{\text{Obtained weight of the product}}{\text{Theoretical weight of the product}} \times 100 \quad (1)$$

The obtained product (14-aryl-14-*H*-dibenzo[*a*,*j*]xanthenes, pale yellow solid) was characterized by m.p, 184–185 °C, and FT-IR (ν = 742, 805, 960, 1076, 1250, 1401, 1456, 1512, 1594, 1628, 2854, 2924, 3061 cm^{-1}.

2.6. Batch adsorption experiment

A series of 150 mL Erlenmeyer flasks were filled with 100 mL of heavy metal ions. 0.03 g MOF was added to each conical flask and shaken in a thermostated shaker at 150 rpm. Then, 10 mL of the solution was collected through centrifugation at 4000 rpm for 10 min. The filtrate was collected in a polyethylene tube and the concentrations of Pb(II), Cu(II) and Cd(II) were determined by dilution. 1 mL from the filtered solution with 2 mL of 4,2-pyridylazo resorcinol (PAR) and 10 mL buffer (pH = 10) were prepared in measuring flask, then the volume was completed by distilled water to 25 mL, and Unicom 5625 UV/Vis Spectrophotometer, PerkinElmer USA was used for the determination of heavy metal ions concentration. The effect of the initial solution pH on metal ion removal was determined for pH values of 3–7 by the batch removal process described above. The pH was adjusted with 0.1 M HNO_3 and 0.1 M NaOH to prepare acidic and neutral solutions, respectively. An adsorption

kinetics study of the removal of Pb(II), Cu(II) and Cd(II) by MOF was carried out at the optimum conditions.

3. Results and discussion

3.1. Characterization

3.1.1. FT-IR analysis. The FTIR spectra of Fig. 1 display a main characteristic peak at ~3450 cm^{-1} assigned for the H–O–H stretching vibrations. The peaks which are observed at 1598 cm^{-1} for Mg-MOF and Fe-MOF, 1646 cm^{-1} of (0.6 : 1) Fe–Mg MOF and 1665 cm^{-1} of (1 : 1) Fe–Mg MOF have been specified for the strong C=O (–COOH) stretching vibration that may be ascribed to the existence of terephthalic acid in the MOF.[29] The appeared peak ~1390 cm^{-1} is due to the C–O stretching vibration. The three peaks at 1015, 1100 and 1145 cm^{-1} were attributed to the bending vibration of the hydroxyl group bound to metal ions (M – OH)[29] and the substitution of the aromatic ring is appeared at 825 cm^{-1}. These results suggest that the structure of Fe-MOF, Mg-MOF and Fe–Mg-MOF contains the basic terephthalic acid skeleton and the carboxyl groups of terephthalic acid are deprotonated. In addition, the bands at 758, 760 and 752 cm^{-1} were ascribed to metal–oxygen vibrations.[30]

3.1.2. X-ray diffraction analysis. The crystallization behaviors of Fe-MOF, Mg-MOF and ((0.6 : 1) and (1 : 1)) Fe–Mg MOF are investigated using XRD analysis and were shown in Fig. 2. XRD patterns characteristic of Fe-MOF are recognized at 2θ = 9.59, 14.31, 18.18, 19.23, 21.85, 24.83, 28.76, 29.70, 33.78, 39.43, 40.34, 41.84, 43.74, 45.25, 46.88, 48.72 and 50.56° (ref. 31) and that of Mg-MOF are recorded at 2θ = 9.33, 12.52, 18.64, 23.68 and 28.24° (ref. 32) confirming the formation of metal–organic framework[33,34] with well-developed crystallinity and without any oxide impurities. From the comparison of the low angle diffraction peaks of Fe–Mg MOF (0.6 : 1) and each of Mg-MOF and Fe-MOF, bimetallic MOF records slight shift toward lower 2θ and the disappearance of the diffraction peaks characteristic for Mg-MOF and Fe-MOF confirming the incorporation of Fe in the as-synthesized architectures. By increasing the Fe : Mg molar ratio to 1 : 1, the intensity of these XRD peaks increases indicated that the as-prepared Fe–Mg MOF showed the typical diffraction pattern of Fe–Mg MOF, which simultaneously possessed characteristic peaks belonging to Mg-MOF and Fe-MOF. This can be attributed to the high dispersion of Fe crystals on the outer cavities of Mg-MOF surface and inside the pores.[35,36] In addition, the observed simultaneous shifts of the XRD patterns to lower and higher angles may be ascribed to the flexibility and/or the breathing effect of Fe-MOF structure.[37–39] By increasing the ratio of Fe : Mg to 1 : 1, the Fe species aggregated on the surface of Mg-MOF which in role decreases the synergistic effect between the two metals and so the intensity of the diffraction peaks characteristic of both Fe and Mg is increased. By applying Scherer eqn (2) for the first peak (111), the crystal size can be easily determined. As seen from the results that tabled in Table 1, the crystal size is decreased by increasing the ratio of Fe : Mg to 0.6 : 1 then begins to slightly increase by increasing the ratio to 1 : 1 confirming the effect of Fe species on Mg-MOF.

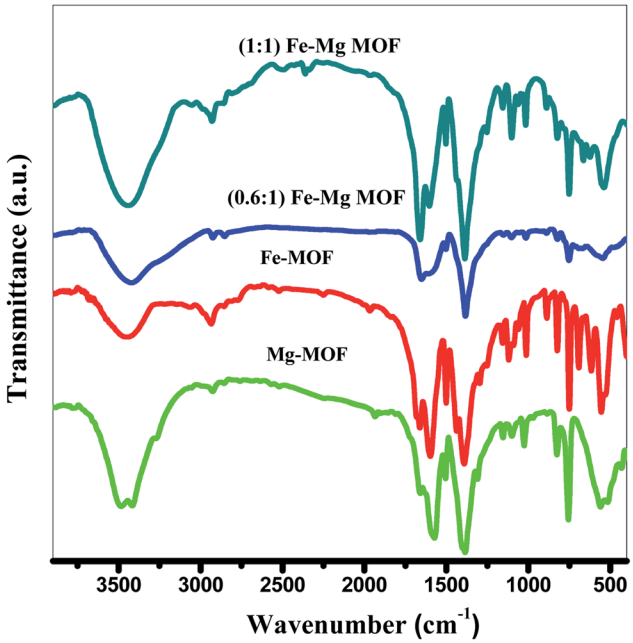

Fig. 1 FTIR spectra of the prepared MOFs.

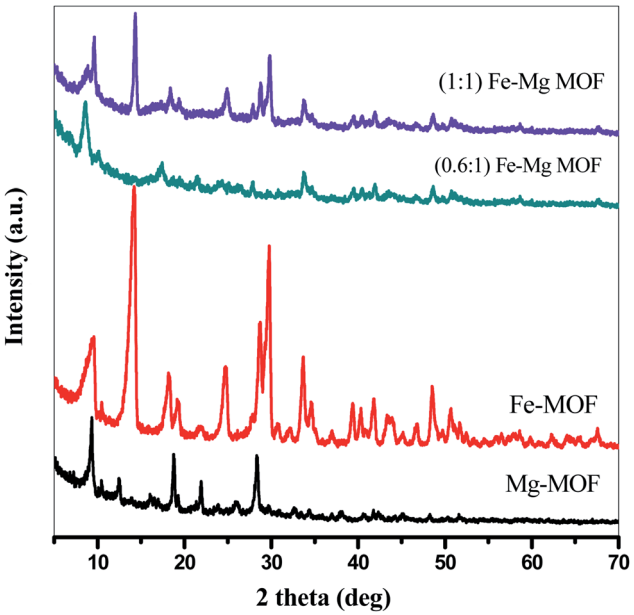

Fig. 2 XRD of the prepared MOFs.

$$D = \frac{0.9\lambda}{\beta \cos \theta} \quad (2)$$

where λ is radiation wavelength ($\lambda = 1.54$ Å), D is crystal size, β is the line breadth (radians) and θ = angle of reflection.

3.1.3. SEM, TEM and EDS studies. The surface morphologies of MOF samples were examined by photographing the surface using scanning and transmission electron microscopes. The images of Mg-MOF and Fe-MOF are shown in Fig. 3A(a, b) and B(a*, b*). As shown from the figures the crystals of Fe-MOF

Table 1 Crystallite size, surface area acidity and activity of the prepared MOFs

Sample name	Crystallite size (nm)		S_{BET} (m^2 g^{-1})	E_i (mV)	No. of acid sites/g × 10^{-19}	Yield (%) of 14-aryl-14-*H*-dibenzo[*a*,*j*]xanthenes
	From XRD peak (111)	From TEM				
Mg-MOF	10.6	11.0–22.3	774	116.2	16.9	38.4
Fe-MOF	12.1	8.0–9.6	983	137.3	28.9	41.4
(0.6 : 1) Fe–Mg MOF	4.5	3.1–3.9	1320	273.1	63.7	93.5
(1 : 1) Fe–Mg MOF	6.1	6.5–10.9	1162	180.5	34.9	72.8

are shaped as a rigid zeotype octahedral structure while that of Mg-MOF appeared as column-like with irregular sizes.[40,41] Fig. 3A(c, d) and B(c*, d*) showed the SEM and TEM images of bimetallic Fe–Mg MOF. In the SEM images; the aggregation of Fe–Mg MOF crystals became more visible which shows a clear differentiation between both single and bimetallic MOF crystals. Fe-MOF with a diameter of 8.0–9.6 nm (from TEM measurements, Table 1) is firstly dispersed in the pores of Mg-MOF with diameter 11.0–22.3 nm then on the external surface. However, in TEM images of (1 : 1) Fe–Mg MOF; the observed larger dark spots on the Mg-MOF surface have resulted from the formation of aggregates of Fe-MOF nanocrystals. Similar agglomerations about bimetallic MOFs were observed in other literature.[42,43] The SEM and TEM images are in good agreement with the XRD results in which for (0.6 : 1) Fe–Mg MOF the peak corresponding to Fe-MOF was found to disappear and on increasing Fe, large aggregates were formed on Mg surface. The EDS spectrum (Fig. 4) of (0.6 : 1) Fe–Mg MOF confirms the presence of both Fe and Mg in the bimetallic MOF.

3.1.4. S_{BET} measurements. The porosity of the MOF materials and BET surface area are examined by N_2 adsorption/desorption analysis at −196 °C. The isotherms, Fig. 5, reveal that all the prepared MOFs show type I isotherms typical of microporous structure. The S_{BET} of Fe-MOF, Mg-MOF, (0.6 : 1) Fe–Mg MOF and (1 : 1) Fe–Mg MOF are 774, 983, 1320 and 1162 m^2 g^{-1}, respectively. As illustrated the bimetallic MOFs exhibit higher surface area than the both of monometallic MOFs. This may be ascribed to the creation of new micropores and consequently new active sites by the presence of both two metals Fe and Mg together in the bimetallic MOF.[1] The surface area of (0.6 : 1) Fe–Mg MOF is high compared with that of (1 : 1) Fe–Mg MOF. This can be explained, as discussed above, due to the synergistic effect between Fe and Mg metals and the high dispersion of Fe crystals inside the pores and on the outer cavities of Mg-MOF surface.[35,36] This synergistic effect decreases in (1 : 1) Fe–Mg MOF material due to the aggregation of Fe species on the surface of Mg-MOF. The BET results confirm the results of XRD, TEM and SEM analysis.

3.2. Surface acidity

The surface acidity of the MOFs was determined using a potentiometric titration method using a basic molecule as *n*-butylamine. The initial electrode potential (E_i) obtained from this technique displays the maximum acid strength of the catalyst surface while the overall issue of acid sites per gram solid catalyst (m_{eq}/g) has been obtained from the domain where a plateau is extended. The acidity measurements resulted from the potentiometric titration curves, Fig. 6 of MOFs catalysts were recorded in Table 1. The following equation successfully used to calculate the overall issue of acid sites/gram catalyst:

$$\frac{\text{Total number of acid sites}}{\text{g}} = \frac{m_{\text{equiv.}}}{\text{g}} \times \frac{N}{1000} \qquad (3)$$

where N is Avogadro's number.

It was proposed that the sites with $E_i > 100$ mV are very strong sites, the sites with $0 < E_i < 100$ mV are strong sites, the sites with

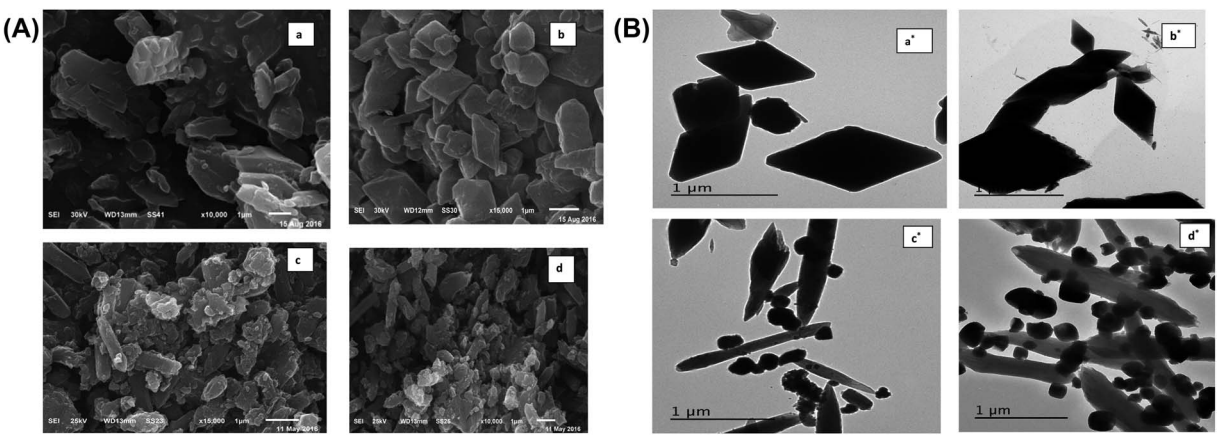

Fig. 3 (A) SEM images of Mg-MOF (a), Fe-MOF (b), (0.6 : 1) Fe–Mg MOF (c) and (1 : 1) Fe–Mg MOF (d). (B) TEM images of Mg-MOF (a*), Fe-MOF (b*), (0.6 : 1) Fe–Mg MOF (c*) and (1 : 1) Fe–Mg MOF (d*).

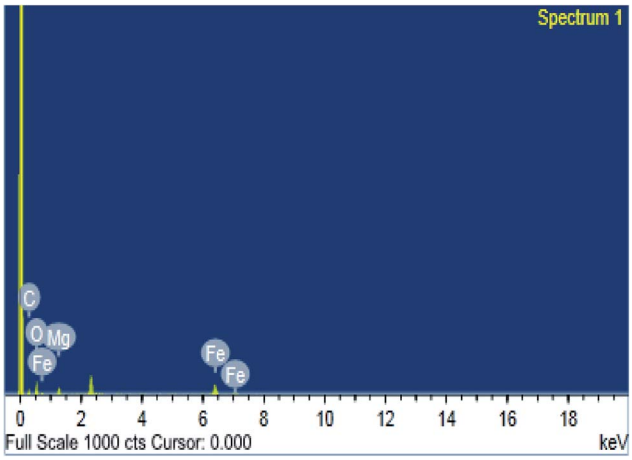

Fig. 4 EDS image of (0.6 : 1) Fe–Mg MOF.

$-100 < E_i < 0$ are weak sites and the sites with $E_i < -100$ mV are very weak sites.[28,44,45] From Table 1 and Fig. 6 and according to the above classification, both pure Mg-MOF and pure Fe-MOF samples exhibit strong acid sites, $E_i = 116.2$ and 137.3 mV, respectively. For bimetallic MOF, the incorporation of Fe-MOF into Mg-MOF increases the surface acidity and the acid strength ($E_i = 273.1$ mV) for the sample (0.6 : 1) Fe–Mg MOF as a result of the high surface area and high synergistic effect between Fe and Mg metals due to the dispersion of Fe-MOF particles on the surface and within the pores of Mg-MOF as evident from XRD, TEM and S_{BET} analysis. The decreases in the surface acidity and the acid strength of (1 : 1) Fe–Mg MOF, ($E_i =$ 180.5 mV) may be related to the decrease in the surface area as a result of the aggregation Fe-MOF species and formation of multilayer on the Mg surface which in role decreases the synergistic effect between the two metals as mentioned above in XRD, SEM, TEM and S_{BET} results.

3.3. Catalytic activity

3.3.1. Synthesis of 14-aryl-14-*H*-dibenzo[*a*,*j*]xanthenes. 14-aryl-14-*H*-dibenzo[*a*,*j*]xanthenes can be synthesized using

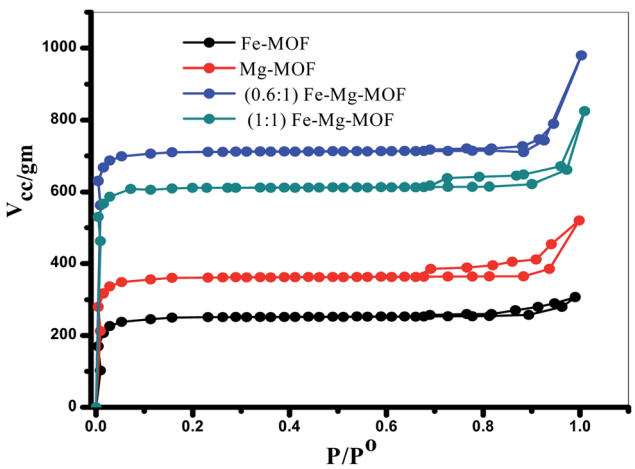

Fig. 5 N_2 adsorption–desorption isotherms of the prepared MOFs.

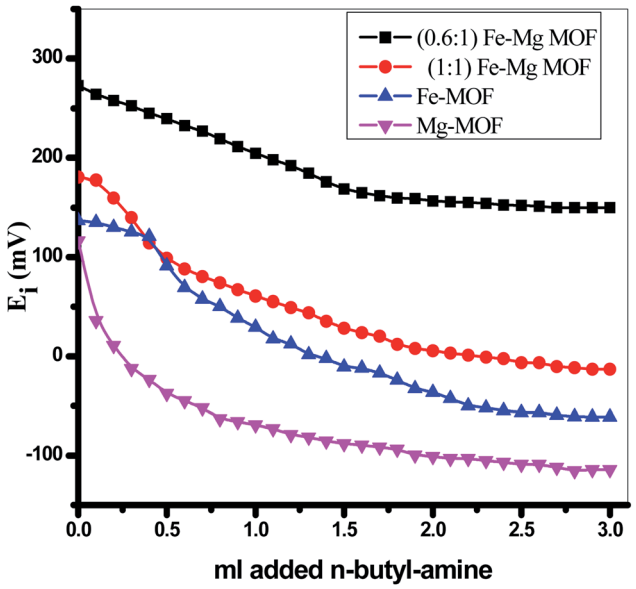

Fig. 6 Nonaqueous potentiometric titration for the prepared MOFs.

benzaldehyde and 2-naphthol in presence of the prepared MOFs. The yield of xanthenes in the presence of pure Mg-MOF crystals was found to be 38.4% while in presence of Fe-MOF was found to be 41.4%, the yield was significantly increased over bimetallic MOF as shown in Fig. 7. The maximum yield (93.5%) was obtained for (0.6 : 1) Fe–Mg MOF catalyst which has the maximum number of acid sites. The yield is improved remarkably using bimetallic system than monometallic ones in a good agreement with the surface acidity and the total number of acid sites. This can be ascribed to a synergetic interaction between Fe and Mg in Fe–Mg MOF which plays an important role in catalytic reactions.[35,46–48] The decrease in the catalytic activity of the sample (1 : 1) Fe–Mg MOF was due to the agglomeration of Fe nanoparticles on the surface of Mg which

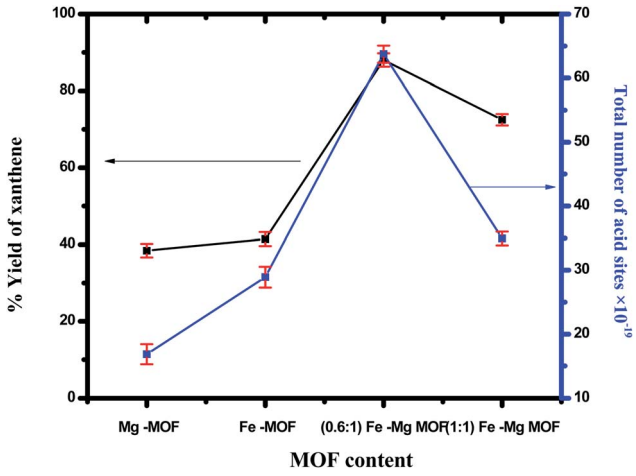

Fig. 7 Effect of the total number of acid sites of the prepared MOF on synthesis of 14-aryl-14-*H*-dibenzo[*a*,*j*]xanthenes. The error bars represent the standard error.

decrease acidity and activity, Fig. 7. The reaction can occur *via* Fe and Mg metals which considered as a Lewis acid catalyst which activates the carbonyl group of the benzaldehyde. Then, a fast Knoevenagel addition was occurred by condensation of one molecule of β-naphthol to provide an intermediate followed by Michael-type addition of the active methylene of the second molecule of β-naphthol to the intermediate followed by cyclization and hydrolysis afforded the final product 14-aryl-14-*H*-dibenzo[*a*,*j*]xanthenes.[49–51]

3.3.2. Reusability of the MOF. From the viewpoint of green chemistry, we tried hard to design a green and reused catalyst. We performed the reusing test of the MOF in the model reaction between benzaldehyde (1 mmol) and 2-naphthol (2 mmol) in the presence of 0.03 g of (0.6 : 1) Fe–Mg MOF at 120 °C. After each run, the MOF was separated, washed with ethanol and dried at 120 °C. From Fig. 8A, (0.6 : 1) Fe–Mg MOF can be recovered and reused in the xanthenes formation reaction four times with remarkably similar activity proving that Fe has been effectively incorporated in the framework of Mg MOF. The FTIR and XRD analyses were determined for the fresh and reused (0.6 : 1) Fe–Mg MOF as shown in Fig. 8B and C. To detect any leached amount of Fe or Mg ions during the reaction, the leaching of the catalysts was tested by taking a small amount of the filtrate after centrifugation during recycling and analyzing it by the atomic absorption spectroscopy. No traces are found from both metals in the filtrate which indicate no leaching process is occurred during the reaction.

Previously reported synthesis of pharmaceutically 14-aryl-14-*H*-dibenzo[*a*,*j*]xanthenes compared with our catalysts showed that the efficiency of Fe–Mg MOF was so higher than that of several reported catalysts *e.g.* nano-$ZnAl_2O_4$,[52] acid activated clay in Kerman Province,[53] graphene oxide-copper ferrite nanocomposite,[54] palladium nanoparticles supported on amino-functionalized MOFs and zinc oxide nanoparticles.[55] The comparison study not only depended on the percentage yield of the desired product but also the condition required optimizing the reaction.

3.4. Adsorption of Pb(II), Cd(II) and Cu(II) ions by Mg, Fe and Fe–Mg MOFs

Pb(II), Cd(II) and Cu(II) ions present in positive forms; therefore, can easily undergo favorable electrostatic interactions with the MOF adsorbents having negatively charged framework (surface). Mg, Fe and Fe–Mg MOF were successfully used to adsorb Pb(II), Cd(II) and Cu(II) ions which are different in ionic radius. The individual influences of solution pH, adsorption time, initial cations concentration and adsorbent dose on the uptake efficiency of Pb(II), Cd(II) and Cu(II) ions by MOF have been studied to detect the optimum range of every single operating factor. In order to achieve this, we noticed the influence resulted by changes in a single parameter while the other operating parameters were maintained constant.

3.4.1. Effect of contact time. Fig. S1† shows the effect of changing the time of adsorption from 10 to 240 min on the adsorption of Pb(II), Cd(II) and Cu(II) ions. The adsorbed amount of metal ions at any time q_t (mg g^{-1}) is calculated by eqn (4):[56]

$$q_t = \frac{(C_0 - C_t)V}{m} \quad (4)$$

where C_0 and C_t are the initial and equilibrium concentration (mg L^{-1}) of the metal ions in the solutions under investigation at the time (t), m is the mass of the MOF and V is the volume of the solution (L).

As shown in Fig. S1,† the removal of Pb(II), Cd(II) and Cu(II) ions by (0.6 : 1) Fe–Mg MOFs began fast then increases noticeably with the prolongation of time until equilibrium is reached at 75 min. There is no obvious variation in the adsorbed cations was observed after 75 min of contact. According to these results, 75 min has been taken as the equilibrium time for Pb(II), Cd(II) and Cu(II) ions in batch adsorption experiments. At the beginning of adsorption, binding (active) sites of adsorbent were freely available to bind adsorbate, which saturated as time proceeds. The exhausted binding sites after saturation repels the coming adsorbate, also the concentration gradient between the solution and solid surface has been changed.[57] Previously studies also have been reported that with the time proceeds the adsorption may decrease due to partial coverage of the adsorbent active sites.[58]

3.4.2. Effect of pH. The solution pH is an important variable influencing the acid–base property of the adsorbent surface. Fig. 9 showed that the adsorption of Pb(II) is increased from (108.4 mg g^{-1}) at pH = 3 to reach maximum (140.6 mg g^{-1}) at pH 5, but the removal of Cd(II) is increased from (44.3 mg g^{-1}) at pH 4 to reach maximum around pH 7 (134.4 mg g^{-1}), while, the removal of Cu(II) is increased from 82.5 mg g^{-1} at pH = 3 to reach 95.6 mg g^{-1} at pH = 5. Thus, the optimum pH is achieved at pH = 5 for Pb(II), Cu(II) and 7 for the removal of Cd(II).[59] At low pH (pH less than 3), MOF offered a positive surface charge, since functional groups of the surface were protonated,[60] which gives rise to electrostatic repulsion among MOF and Pb(II), Cu(II) and Cd(II) resulting in low cationic metal ions removal. When the pH of the solution is increased, a negative surface charge appeared on the MOF surface because of the deprotonating of function groups which was favorable for the surface electrostatic attraction of positively charged Pb(II), Cu(II) and Cd(II) found in solution which make the ion exchange process occurred. In acidic solution, hydrated hydrogen ions (H_3O^+) competed with Pb(II), Cd(II) and Cu(II) on the available adsorption sites. As the pH increases, the concentration of H_3O^+ decreases resulting in increasing the adsorption rate of Pb(II), Cd(II) and Cu(II). Moreover, increasing the adsorption capacity with increasing the pH is due to the greater stability of MOF structure in addition to the increase of the negatively charged active centers. Furthermore, considering precipitation of both ($Pb(OH)^+$ and $Pb(OH)_2$), ($Cu(OH)^+$ and $Cu(OH)_2$) that appear at pH > 5 and precipitation of both ($Cd(OH)^+$ and $Cd(OH)_2$) that seem at pH > 7.

3.4.3. Adsorbent dose. The effect of adsorbents weight is one of the most significant factors that affect the adsorption. In this test different amounts of MOFs (10–70 mg) were added to 50 mL solution with concentration of (100 mg L^{-1}) and appropriate pH, then shacked for 2 h at 25 °C and by UV/Vis spectrophotometer, the adsorption of Pb(II), Cd(II) and Cu(II) were

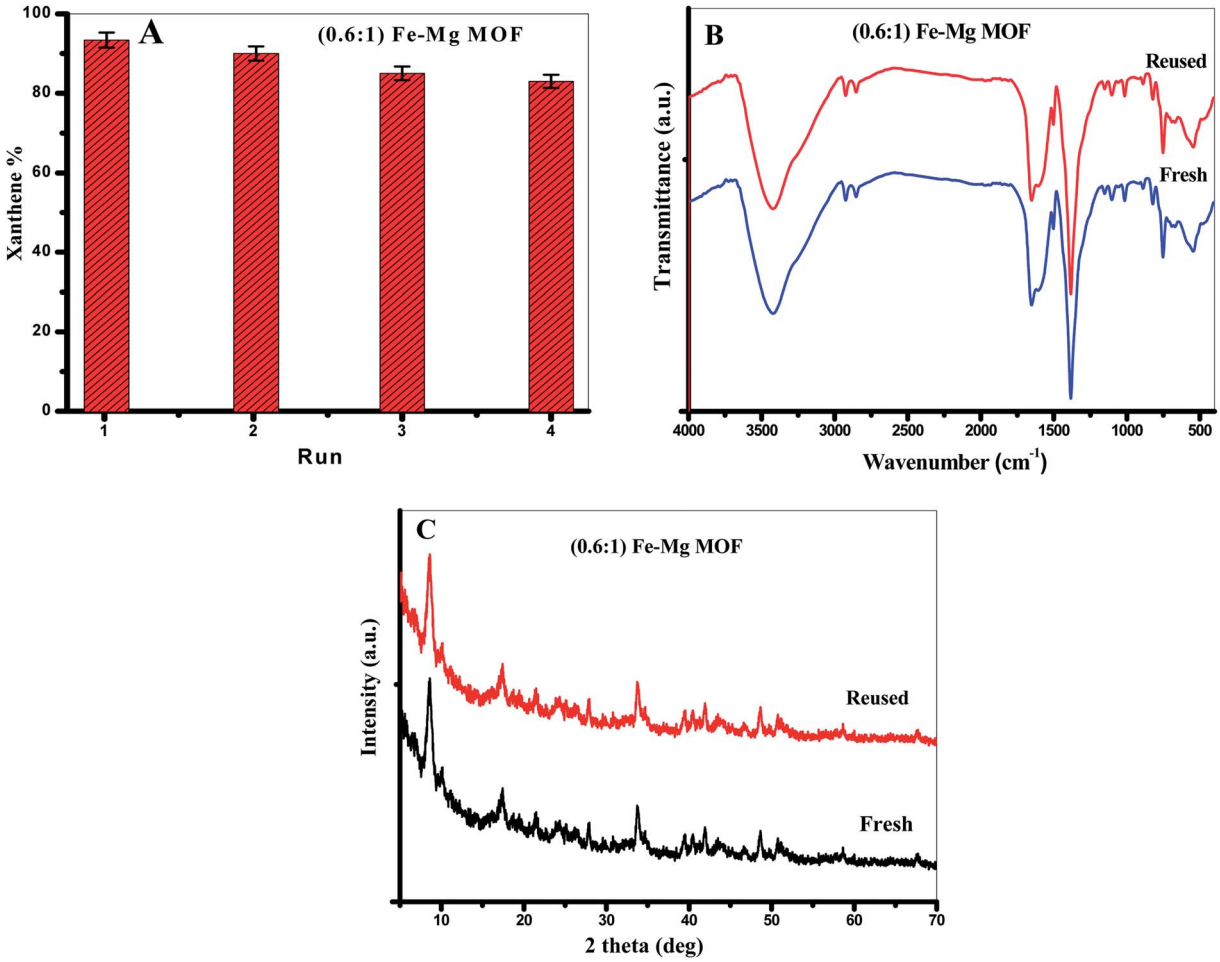

Fig. 8 (A) The reusability of (0.61) Fe–Mg MOF in the synthesis of xanthenes, (B) XRD and (C) FTIR of the fresh and reused (0.61) Fe–Mg MOF. The error bars represent the standard error.

evaluated. Fig. S2,† shows the adsorption amount as a function of the mass of MOFs. The experimental results demonstrated that the adsorption is increased with the increase in the weight of MOFs catalyst from (10–50 mg) and then almost constant. This is may be due to the increase of the number of the deprotonating function groups on the solid MOF by increasing its weight up to 50 mg which was favorable for the surface electrostatic attraction of positively charged cations.[61–63] The almost constant adsorption after 50 mg of MOF may be attributed to the saturation of the surface active sites available for the adsorbed cations.

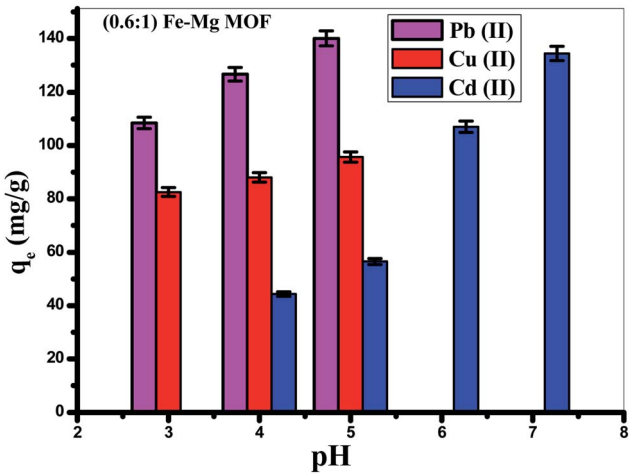

Fig. 9 Effect of pH on the removal of Pb(II), Cd(II) and Cu(II) ions by (0.6 : 1) Fe–Mg MOF sample. The error bars represent the standard error.

3.4.4. Effect of the initial concentration of the heavy metal ions. The adsorption isotherms of the Pb(II), Cd(II) and Cu(II) by MOFs were studied in a series of batches using various initial concentrations ranging from (50–200 mg L^{-1}) at 25 °C. From Fig. S3,† It is clear that the adsorption increases with the increase in the initial concentrations of the heavy metal ions up to 150 mg L^{-1} then almost steady constant. This can be ascribed to the saturation of most available active sites of MOFs with raising the initial concentration of Pb(II), Cd(II) and Cu(II).[59] Cations adsorption efficiency were significantly higher for initial concentration up to 150 mg L^{-1} due to plenty of freely active sites on the adsorbent surface which has been saturated at extremely higher cation concentrations and as a result, the

adsorption slowed increases due to the competition between ions for the available binding sites.[8,57]

3.4.5. Adsorption isotherms. For a solid–liquid system, one of the most important physico-chemical studies in the characterization of sorption behavior is the equilibrium isotherm of sorption which used to characterize the experimental adsorption data. The Langmuir isotherm is the most applied adsorption model and aspects monolayer sorption behavior on the adsorbent surface which contains a homogeneous and definite number of active sites.[64] The model generally expressed in the well-known form represented in the following equation as:

$$q_e = \frac{K_L C_e}{1 + q_m C_e} \quad (5)$$

A linear form of this model expression is:

$$\frac{C_e}{q_e} = \frac{1}{K_L q_{max}} + \frac{C_e}{q_{max}} \quad (6)$$

where C_e (mg L^{-1}) is the equilibrium concentration of the adsorbed molecule; q_e (mg g^{-1}) is the adsorption capacity of the adsorbent at equilibrium per unit mass of adsorbent; q_{max} (mg g^{-1}) indicates the theoretical sorption capacity and K_L in L mg^{-1} is the Langmuir sorption isotherm constant. One of the most important descriptions of the Langmuir isotherm equation is the dimensionless separation factor (R_L), represented in the equation as:[65]

$$R_L = \frac{1}{1 + K_L C_0} \quad (7)$$

where K_L in L mg^{-1} is the Langmuir sorption constant and C_0 in mg L^{-1} is the initial concentration of the adsorbed molecules. The R_L values describe the isotherm type to be either irreversible ($R_L = 0$), linear ($R_L = 1$), unfavorable ($R_L > 1$) or favorable ($0 < R_L < 1$). On the other hand, Freundlich isotherm model is represented by the well-known logarithmic form which expressed in the following equation:[66,67]

$$q_e = K_F C_e^{1/n} \quad (8)$$

A linear form of this expression can be represented as follows:

$$\ln q_e = (1/n)\ln C_e + \ln K_F \quad (9)$$

where n and K_F are the Freundlich isotherm exponents. K_F describes the adsorption or distribution coefficient giving an indication of the definite quantity of the adsorbed molecule on an adsorbent surface at equilibrium while n indicates the favorability of the adsorption isotherm and measure the surface heterogeneity or adsorption intensity. The process is more heterogeneous when the value of $1/n$ gets nearer to zero. A value of $1/n$ lower than unity is indicative of Langmuir isotherm while $1/n$ above unity indicating of co-operative sorption.[68] Langmuir and Freundlich sorption isotherms for Pb(II), Cd(II) and Cu(II) using (0.6 : 1) Fe–Mg MOF as adsorbent are seen in Fig. S4.† The correlation factor coefficients, R^2 and isotherm parameters are calculated and recorded at Table 2. The Langmuir model with R^2 factor ranging from 0.9980 to 9982 for Pb(II), 0.981 to 0.998 for Cd(II) and 0.985 to 0.999 for Cu(II), respectively, represents the accurate fit of the experimental data and more acceptable than that of Freundlich isotherm. It gives an indication of the monolayer adsorption of Pb(II), Cd(II) and Cu(II) ions on the homogeneous surface of Fe–Mg MOF adsorbent. The maximum monolayer capacity obtained from Langmuir model for the uptake of Pb(II), Cd(II) and Cu(II) is found to be 196, 191 and 175 mg g^{-1}, respectively. Moreover, the dimensionless separation constant R_L values between 0.033–0.213, 0.117–0.293 and 0.020–0.227 for of Pb(II), Cd(II) and Cu(II) respectively indicate the favorability of the sorption process for the three cations, also the value of $1/n$ lower than unity is indicative of Langmuir isotherm as shown in Table 2. Moreover, it is obviously from the adsorption figures and Table 2 that the (0.6 : 1) Fe–Mg MOF material show the better adsorption efficiency among the other prepared MOFs. This can be explained on the basis of increasing surface area due to the synergistic effect between the two metals and creation of new active sites that facilitate and improve the adsorption efficiency in this sample.

3.4.6. Adsorption kinetics. In order to design a plan for adsorption treatment, the rate at which adsorbate rejected from an aqueous solution is important to be predicted. The two well-known models pseudo 1st order and pseudo 2nd order were applied to the experimental data of the adsorption processes to evaluate the adsorption kinetics.[2,64] The integrated and linear forms of these kinetic models are seen respectively in the following equations:

$$\ln(q_e - q_t) = \ln q_e - k_1 t \quad (10)$$

$$\frac{t}{q_t} = \frac{1}{k_2 q_e^2} + \frac{1}{q_e} t \quad (11)$$

where k_1 (min^{-1}) and k_2 in g (mg min)$^{-1}$ are respectively the adsorption rate constants of the 1st and 2nd pseudo-order; q_e and q_t in mg g^{-1} are respectively the quantities of adsorbate at equilibrium and time (t). The adsorption kinetic parameters are collected in Table 3. The determined R^2 factor for the pseudo 2nd order model is closer to unity than that of the pseudo 1st model, Table 3, and the values of $q_{e(Exp)}$ of the adsorbed cations are in good agreement with that of q_{e2}, therefore these sorption systems follow the pseudo 2nd order kinetic model predominantly.

3.4.7. Mechanism of adsorption. Adsorption mechanism is generally described through three stages are as follows:

(i) Movement of adsorbate molecules towards the external surface of the adsorbent from the bulk of the solution (film diffusion).

(ii) Particle diffusion, which involves the transfer of ions to the intra particular active sites from the surface.

(iii) Finally adsorption of ions by the contact with active sites in the adsorbent.

The third step does not consider the rate which controls steps because it is a very rapid, consequently the rate which controls steps mainly either particle diffusion or film diffusion.

Weber and Morris who first suggested the model of intra-particle diffusion, which summarized that the adsorption was

Table 2 Langmuir and Freundlich parameter for adsorption of heavy metals on the prepared MOFs

Sample	Heavy metal ions	Langmuir isotherm				Freundlich isotherm		
		q_{max} (mg g^{-1})	K_L (L mg^{-1})	R^2	R_L	K_F (mg g^{-1})	n	R^2
Mg-MOF	Pb(II)	158	0.237	0.97243	0.078	1.61	2.32	0.96677
Fe-MOF		179	0.074	0.95238	0.213	2.88	2.27	0.90465
0.6 : 1 Fe–Mg MOF		196	0.582	0.99980	0.033	4.28	5.37	0.98474
1 : 1 Fe–Mg MOF		186	0.282	0.99741	0.066	3.98	3.70	0.97055
Mg-MOF	Cd(II)	130	0.048	0.98339	0.293	1.36	2.09	0.96358
Fe-MOF		163	0.103	0.96483	0.163	3.78	2.17	0.96402
0.6 : 1 Fe–Mg MOF		191	0.151	0.97059	0.117	3.85	4.32	0.91991
1 : 1 Fe–Mg MOF		185	0.145	0.94089	0.121	3.73	2.15	0.93427
Mg-MOF	Cu(II)	119	0.078	0.96236	0.204	3.34	1.02	0.92998
Fe-MOF		161	0.290	0.97734	0.065	3.43	1.03	0.97205
0.6 : 1 Fe–Mg MOF		175	0.079	0.97512	0.020	4.47	2.57	0.96631
1 : 1 Fe–Mg MOF		172	0.068	0.95824	0.227	3.89	2.04	0.94908

Table 3 Kinetic parameters for adsorption heavy metals on the prepared MOFs

Sample	Heavy metal ions	$q_{e(Exp)}$ (mg g^{-1})	Pseudo-first-order-kinetic-model			Pseudo-second-order-kinetic-model		
			q_{e1} (mg g^{-1})	k_1 (min^{-1})	R^2	q_{e2} (mg g^{-1})	k_2 (g mg^{-1} min^{-1})	R^2
Mg-MOF	Pb(II)	130	124.66	0.00974	0.99133	130.55	0.000105	0.98251
Fe-MOF		179	167.28	0.00647	0.97538	178.57	0.000052	0.97784
0.6 : 1 Fe–Mg MOF		196	191.48	0.00567	0.96155	191.48	0.000056	0.95771
1 : 1 Fe–Mg MOF		186	190.70	0.00554	0.99424	187.97	0.000057	0.96896
Mg-MOF	Cd(II)	130	124.66	0.00973	0.98251	130.55	0.000104	0.99133
Fe-MOF		163	130.89	0.00757	0.97035	163.67	0.000267	0.99945
0.6 : 1 Fe–Mg MOF		191	192.22	0.00457	0.97504	190.84	0.000045	0.97883
1 : 1 Fe–Mg MOF		185	173.93	0.00550	0.90459	188.68	0.000040	0.99620
Mg-MOF	Cu(II)	119	111.93	0.00333	0.96885	119.19	0.000151	0.98877
Fe-MOF		161	128.88	0.00753	0.99945	163.67	0.000267	0.99988
0.6 : 1 Fe–Mg MOF		172	164.23	0.01212	0.95995	172.12	0.000135	0.99157
1 : 1 Fe–Mg MOF		175	165.25	0.00977	0.96885	176.68	0.000125	0.96477

proportional to the square root of the contact time[69] as demonstrated from the following equation:

$$q_t = K_d t^{\frac{1}{2}} + C \quad (12)$$

3.4.8. Boyd model. To differentiate between particle diffusion and film diffusion in order to identify the slowest step in the process of adsorption kinetic equation Boyd was utilized,[70] which is represented as:

$$F(t) = 1 - \left(\frac{6}{\pi(22)^2}\right)\exp(-Bt) \quad (13)$$

Both intraparticle diffusion and Boyd plots are applied in order to predict the rate limiting step. The lines don't pass

Table 4 Comparison of the adsorption efficiency of our catalyst with the previously reported articles

Catalyst	Heavy metal ion	Isotherm	q_{max} (mg g^{-1})	Ref.
Iron oxide	Pb(II)	Freundlich	36.00	71
G-C_3N_4	Pb(II)	Langmuir	71.10	72
Cellulose	Cu(II)	Langmuir	52.32	73
Iron nanoparticles	Cu(II)	Langmuir	55.20	74
Biochars	Cd(II)	Freundlich	13.24	75
Graphene	Cd(II)	Langmuir	57.60	76
Plantain peels	Cd(II)	Langmuir	70.92	77
Fe–Mg MOF	Pb(II)	Langmuir	196	This study
	Cd(II)		191	
	Cu(II)		175	

through the origin in intraparticle diffusion plot Fig. S5A,† subsequently; the rate limiting step is not only intraparticle diffusion and indicates the effect of film diffusion (boundary layer diffusion). It is a controlled adsorption process for all samples by film diffusion, due to the plots of Boyd are linear but do not pass through the origin the parameters of intraparticle diffusion and Boyd plot for adsorption heavy metals Pb(II), Cd(II) and Cu(II) ions onto investigated catalysts are displayed in Fig. S5B.†

3.4.9. Comparison studies with various previously reported adsorbents applied for removal of Pb(II), Cd(II) and Cu(II). A comparison study was made between the results achieved in this work for the removal of Pb(II), Cd(II) and Cu(II) through (0.6 : 1) Fe–Mg MOF with those obtained by other adsorbents reported previously in the literature and listed in Table 4. The results demonstrated that 0.6 : 1 Fe–Mg MOF among other various adsorbents mentioned above behaves as an effective adsorbent for adsorption of heavy metal cations with respect to maximum adsorption capacity (mg g^{-1}).

4. Conclusion

This paper offers an Fe–Mg MOF with various advantages such as being easily prepared in larger amounts, high catalytic activity, straight forward synthetic route under mild conditions, simple handling and an easy recovery without losing its activity which makes it an eco-friendly, green and efficient catalyst. Mg-MOF, Fe-MOF and Fe–Mg-MOF were prepared successfully, characterized using sets of different techniques *e.g.* XRD, FT-IR, SEM, EDS analysis and TEM. The formation of a bimetallic MOF sharply increased the surface acidity and the catalytic activity. The catalytic activity of the formation of 14-aryl-14-*H*-dibenzo[*a*,*j*]xanthenes was related to the acidity of the catalysts. The prepared MOFs were used for removal of Pb(II), Cd(II) and Cu(II) ions from their aqueous solutions. The effect of the experimental parameters such as pH, initial concentration, contact time and MOF weight on the adsorption of Pb(II), Cd(II) and Cu(II) were studied. Both Langmuir and Freundlich isotherm models were used to analyze the equilibrium.

Conflicts of interest

There are no conflicts to declare.

References

1 W. S. Abo El-Yazeed and A. I. Ahmed, *RSC Adv.*, 2019, **9**, 18803–18813.
2 J. Zhang, Z. Xiong, C. Li and C. Wu, *J. Mol. Liq.*, 2016, **221**, 43–50.
3 I. Ahmed and S. H. Jhung, *Mater. Today*, 2014, **17**, 136–146.
4 W. Lu, Z. Wei, Z.-Y. Gu, T.-F. Liu, J. Park, J. Park, J. Tian, M. Zhang, Q. Zhang, T. Gentle, M. Bosch and H.-C. Zhou, *Chem. Soc. Rev.*, 2014, **43**, 5561–5593.
5 J. J-Alcaniz, R. Gielisse, A. B. Lago, E. V. R-Fernandez, P. S-Crespo, T. Devic, N. Guillou, C. Serre, F. Kapteijn and J. Gascon, *Catal. Sci. Technol.*, 2013, **3**, 2311–2318.
6 S. H. Jhung, N. A. Khan and Z. Hasan, *CrystEngComm*, 2012, **14**, 7099–7109.
7 M. O. Rodrigues, M. V. De Paula, K. A. Wanderley, I. B. Vasconcelos, S. Alves and T. A. Soares, *Int. J. Quantum Chem.*, 2012, **112**, 3346–3355.
8 S. A. El-Hakam, S. E. Samra, S. M. El-Dafrawy, A. A. Ibrahim, R. S. Salama and A. I. Ahmed, *RSC Adv.*, 2018, **8**, 20517–20533.
9 X.-F. Wang, X.-Z. Song, K.-M. Sun, L. Cheng and W. Ma, *Polyhedron*, 2018, **152**, 155–163.
10 J. A. Villajos, G. Orcajo, C. Martos, J. A. Botas, J. Villacanas and G. Calleja, *Int. J. Hydrogen Energy*, 2015, **40**, 5346–5352.
11 P. Iniyavan, S. Sarveswari and V. Vijayakumar, *Tetrahedron Lett.*, 2015, **56**, 1401–1406.
12 B. Xu, D. Bi, Y. Hua, P. Liu, M. Cheng and M. Grätzel, *Energy Environ. Sci.*, 2016, **9**, 873–877.
13 G. Shen, L. Zhao, Y. Wang, W. Xia, M. Yang and T. Zhang, *RSC Adv.*, 2016, **6**, 84748–84751.
14 H. Naeimi and Z. Ansarian, *J. Taiwan Inst. Chem. Eng.*, 2018, 1–8.
15 J. Safari, P. Aftabi, M. Ahmadzadeh, M. Sadeghi and Z. Zarnegar, *J. Mol. Struct.*, 2017, **114215**, 33–39.
16 P. Bansal, N. Kaur, C. Prakash and G. R. Chaudhary, *Vacuum*, 2018, **157**, 9–16.
17 V. S. R. Ganga, M. K. Choudhary, R. Tak, P. Kumari, S. H. R. Abdi, R. I. Kureshy and N. H. Khan, *Catal. Commun.*, 2017, **945**, 5–8.
18 S. H. Huo and X. P. Yan, *Analyst*, 2012, **137**(15), 3445–3451.
19 Y. G. Abou El-Reash, A. M. Abdelghany and A. Abd Elrazak, *Int. J. Biol. Macromol.*, 2016, **86**, 789–798.
20 Y. Ibrahim, E. Abdulkarem, V. Naddeo, F. Banat and S. W. Hasan, *Sci. Total Environ.*, 2019, **69010**, 167–180.
21 A. M. Youssef, A. I. Ahmed, M. I. Amin and U. A. El-Banna, *Desalin. Water Treat.*, 2015, **54**, 1694–1707.
22 M. I. Nandasiri, S. R. Jambovane, B. P. McGrail, H. T. Schaef and S. K. Nune, *Chem. Rev.*, 2016, **311**, 38–52.
23 C. R. Aguiar, É. Fontana, J. A. Valle, A. A. Souza, A. F. Morgado and S. Souza, *Can. J. Chem. Eng.*, 2016, **94**, 947–955.
24 A. M. Anielak and R. Schmidt, *Pol. J. Environ. Stud.*, 2011, **20**, 15–19.
25 M. Monier, D. A. Abdel-Latif and Y. G. Abou El-Reash, *J. Colloid Interface Sci.*, 2016, **469**, 344–354.
26 N. V. P. Aguilar, E. M. Sandoval and J. R. R. Mendez, *J. Nanopart. Res.*, 2010, **12**, 467–480.
27 Y. Gu, D. Xie, Y. Wang, W. Qin, H. Zhang, G. Wang, Y. Zhang and H. Zhao, *Chem. Eng. J.*, 2019, **357**, 579–588.
28 A. I. Ahmed, S. A. El-Hakam, A. S. Khder and W. S. Abo El-Yazeed, *J. Mol. Catal. A: Chem.*, 2013, **366**, 99–108.
29 Z. Zhang, Z. Z. Yao, S. Xiang and B. Chen, *Energy Environ. Sci.*, 2014, **7**, 2868–2899.
30 Z. Li, S. Deng, G. Yu, J. Huang and V. C. Lim, *Chem. Eng. J.*, 2010, **161**, 106–113.
31 Z. Zhang, X. Li, B. Liu, Q. Zhao and G. Chen, *RSC Adv.*, 2016, **6**, 4289–4295.
32 Q. G. Zhai, X. Bu, C. Mao, X. Zhao and P. Feng, *J. Am. Chem. Soc.*, 2016, **138**, 2524–2527.

33 M. N. Cele, H. B. Friedrich and M. D. Bala, *Catal. Commun.*, 2014, **57**, 99–102.
34 X. Yi, W. Dong, X. Zhang, J. Xie and Y. Huangm, *Anal. Bioanal. Chem.*, 2016, **408**, 8805–8812.
35 W. Yu, Y. P. Hsu and C. S. Tan, *Appl. Catal., B*, 2016, **196**, 185–192.
36 Y. Miao, S. Li, L. Gao and G. Xiao, *Mol. Catal.*, 2017, **436**, 128–137.
37 M. H. Pham, G. T. Vuong, A. T. Vu and T. O. Do, *Langmuir*, 2011, **27**, 15261–15267.
38 M. Ma, A. Betard, I. Weber, N. S. Al-Hokbany, R. A. Fischer and N. N. Metzler, *Cryst. Growth Des.*, 2013, **13**, 2286–2291.
39 A. K. Singh and A. K. Singh, *Spectrochim. Acta, Part A*, 2012, **96**, 986–991.
40 J. Tang, M. Yang, M. Yang, J. Wang, W. Dong and G. Wang, *New J. Chem.*, 2015, **39**, 4919–4923.
41 L. Yang, Y. Bai, H. Zhang, J. Geng, Z. Shao and B. Yia, *RSC Adv.*, 2017, **7**, 22610–22618.
42 A. M. Ebrahim and T. J. Bandosz, *ACS Appl. Mater. Interfaces*, 2013, **5**, 10565–10573.
43 J. Yang, C. Zheng, P. Xiong, Y. Li and M. Wei, *J. Mater. Chem. A*, 2014, **2**, 19005–19010.
44 A. I. Ahmed, S. E. Samra, S. A. El-Hakam, A. S. Khder, H. Z. El-Shenawy and W. S. Abo El-Yazeed, *Appl. Surf. Sci.*, 2013, **282**, 217–225.
45 A. I. Ahmed, S. A. El-Hakam, M. A. Abd Elghany and W. S. Abo El-Yazeed, *Appl. Catal., A*, 2011, **407**, 40–48.
46 T. A. Maark and A. A. Peterson, *J. Phys. Chem. C*, 2014, **118**, 4275–4281.
47 L. Ai, X. Liu and J. Jiang, *J. Alloys Compd.*, 2014, **625**, 164–170.
48 R. Mohammadi, E. Eidi, M. Ghavami and M. Z. Kassaee, *J. Mol. Catal. A: Chem.*, 2014, **393**, 309–316.
49 H. Naeimi and Z. S. Nazif, *Appl. Catal., A*, 2014, **477**, 132–140.
50 J. Mondal, M. Nandi, A. Modak and A. Bhaumik, *J. Mol. Catal. A: Chem.*, 2012, **363–364**, 254–264.
51 J. Safari, P. Aftabi, M. Ahmadzadeh, M. Sadeghi and Z. Zarnegar, *J. Mol. Struct.*, 2017, **1142**, 33–39.
52 T. R. Mandlimath, B. Umamahesh and K. I. Sathiyanarayanan, *J. Mol. Catal. A: Chem.*, 2014, **391**, 198–207.
53 H. Rouhani, A. Sarrafi and M. Tahmooresi, *Chem. Eng. Commun.*, 2016, **203**, 289–299.
54 A. Kumar, L. Rout, L. S. K. Achary, R. S. Dhaka and P. Dash, *Sci. Rep.*, 2017, **7**, 42975–42993.
55 R. Kardanpour, R. S. Tangestaninejad, V. Mirkhani, M. Moghadam, I. Mohammadpoor-Baltork, A. R. Khosropour and F. Zadehahmadi, *J. Organomet. Chem.*, 2014, **761**, 127–133.
56 S. Wang, C. W. Ng, W. Wang, Q. Li and Z. Hao, *Chem. Eng. J.*, 2012, **197**, 34–40.
57 M. K. Uddin, *Chem. Eng. J.*, 2017, **308**, 438–462.
58 B. Das, N. K. Mondal, R. Bhaumik and P. Roy, *Int. J. Environ. Sci. Technol.*, 2014, **11**, 1101–1114.
59 J. H. Deng, X. R. Zhang, G. M. Zeng, J. L. Gong, Q. Y. Niu and J. Liang, *J. Chem. Eng.*, 2013, **226**, 189–200.
60 P. Shao, D. Liang, L. Yang, H. Shi, Z. Xiong, L. Ding, X. Yin, K. Zhang and X. Luo, *J. Hazard. Mater.*, 2020, **387**, 121676.
61 W. I. Mortada, I. M. M. Kenawy, Y. G. Abou El-Reash and A. A. Mousa, *Int. J. Biol. Macromol.*, 2017, **101**, 490–501.
62 I. M. M. Kenawy, W. I. Mortada, Y. G. Abou El-Reash and A. H. Hawwas, *Can. J. Chem.*, 2016, **94**, 221–228.
63 S. Hei, Y. Jin and F. Zhang, *J. Chem.*, 2014, 546956.
64 N. Murakami, N. Takebe, T. Tsubota and T. Ohno, *J. Hazard. Mater.*, 2012, **212**, 83–87.
65 H. Li, N. An, G. Liu, J. Li, N. Liu, M. Jia, W. Zhang and X. Yuan, *J. Colloid Interface Sci.*, 2016, **466**, 343–351.
66 M. R. Sohrabi, Z. Matbouie, A. A. Asgharinezhad and A. Dehghani, *Microchim. Acta*, 2013, **180**, 589–597.
67 M. R. Sohrabi, *Microchim. Acta*, 2014, **181**, 435–444.
68 P. Shao, L. Ding, J. Luo, Y. Luo, D. You, Q. Zhang and X. Luo, *ACS Appl. Mater. Interfaces*, 2019, **11**(33), 29736–29745.
69 X. Yin, P. Shao, L. Ding, Y. Xi, K. Zhang, L. Yang, H. Shi and X. Luo, *Environ. Sci.: Nano*, 2019, 3307–3315.
70 H. Yu, P. Shao, L. Fang, J. Pei, L. Ding, S. G. Pavlostathis and X. Luo, *Chem. Eng. J.*, 2019, **359**, 176–185.
71 N. N. Nassar, *J. Hazard. Mater.*, 2010, **184**, 538–546.
72 R. Hu, X. K. Wang, S. Y. Dai, D. D. Shao, T. Hayat and A. Alsaedi, *Chem. Eng. J.*, 2015, **260**, 469–477.
73 N. Zhang, G. L. Zang, C. Shi, H. Q. Yu and G. P. Sheng, *J. Hazard. Mater.*, 2016, **316**, 11–18.
74 X. Weng, X. Jin, J. Lin, R. Naidu and Z. Chen, *Ecol. Eng.*, 2016, **97**, 32–39.
75 W. K. Kim, T. Shim, Y. S. Kim, S. Hyun, C. Ryu, Y. K. Park and J. Jung, *Bioresour. Technol.*, 2013, **138**, 266–270.
76 Y. Shen and B. L. Chen, *Environ. Sci. Technol.*, 2015, **49**, 7364–7372.
77 Z. N. Garba, N. I. Ugbaga and A. K. Abdullahi, *J. Basic Appl. Sci.*, 2016, **5**, 170–179.